HHS Public Access

Author manuscript

Acta Biomater. Author manuscript; available in PMC 2018 July 03.

Published in final edited form as:

Acta Biomater. 2014 August ; 10(8): 3449–3462. doi:10.1016/j.actbio.2014.04.018.

Cardiac differentiation of cardiosphere-derived cells in scaffolds mimicking morphology of the cardiac extracellular matrix

Yanyi Xu[a], **Sourav Patnaik**[b], **Xiaolei Guo**[a], **Zhenqing Li**[a], **Wilson Lo**[c], **Ryan Butler**[d], **Andrew Claude**[d], **Zhenguo Liu**[e], **Ge Zhang**[f], **Jun Liao**[b], **Peter M. Anderson**[a], and **Jianjun Guan**[a,*]

[a]Department of Materials Science and Engineering, The Ohio State University, Columbus, OH 43210, USA

[b]Department of Agricultural & Biological Engineering, Mississippi State University, Starkville, MS 39672, USA

[c]Department of Biochemistry, The Ohio State University, Columbus, OH 43210, USA

[d]Department of Clinical Science, Mississippi State University, Starkville, MS 39672, USA

[e]Davis Heart and Lung Research Institute, The Ohio State University, Columbus, OH 43210, USA

[f]Department of Biomedical Engineering, University of Akron, Akron, OH 44325, USA

Abstract

Stem cell therapy has the potential to regenerate heart tissue after myocardial infarction (MI). The regeneration is dependent upon cardiac differentiation of the delivered stem cells. We hypothesized that timing of the stem cell delivery determines the extent of cardiac differentiation as cell differentiation is dependent on matrix properties such as biomechanics, structure and morphology, and these properties in cardiac extracellular matrix (ECM) continuously vary with time after MI. In order to elucidate the relationship between ECM properties and cardiac differentiation, we created an in vitro model based on ECM-mimicking fibers and a type of cardiac progenitor cell, cardiosphere-derived cells (CDCs). A simultaneous fiber electrospinning and cell electrospraying technique was utilized to fabricate constructs. By blending a highly soft hydrogel with a relatively stiff polyurethane and modulating fabrication parameters, tissue constructs with similar cell adhesion property but different global modulus, single fiber modulus, fiber density and fiber alignment were achieved. The CDCs remained alive within the constructs during a 1 week culture period. CDC cardiac differentiation was dependent on the scaffold modulus, fiber volume fraction and fiber alignment. Two constructs with relatively low scaffold modulus, ~50–60 kPa, most significantly directed the CDC differentiation into mature cardiomyocytes as evidenced by gene expressions of cardiac troponin T (cTnT), calcium channel (CACNA1c) and cardiac myosin heavy chain (MYH6), and protein expressions of cardiac troponin I (cTnI) and connexin 43 (CX43). Of these two low-modulus constructs, the extent of differentiation was greater for lower fiber alignment and higher fiber volume fraction. These results suggest that cardiac ECM properties may have an effect on cardiac differentiation of delivered stem cells.

*Corresponding author. Tel.: +1 614 292 9743., guan.21@osu.edu (J. Guan).

Keywords

Matrix modulus; Cardiosphere-derived cells; Cardiac differentiation; Stem cell therapy

1. Introduction

Myocardial infarction (MI) affects more than 8 million Americans [1]. MI causes massive heart cell death and heart function decrease. Various therapeutic strategies have been used to treat MI [1–8]. However, normal heart function cannot be restored after MI since cardiomyocytes are less proliferative and endogenous cells are unable to produce sufficient cardiomyocytes for effective regeneration. Stem cell therapy is a potential approach to regenerate heart tissue [2–10]. It delivers stem cells to the damaged areas (scar tissue) where they differentiate into cardiomyocytes. However, various animal studies and clinical trials have shown that the success rate for differentiation is low and it therefore remains impractical for widespread clinical application [2–11]. Identifying and addressing the causes for the low success rate is needed for heart tissue regeneration.

The causes of low differentiation are not completely clear. The harsh biochemical environment initiated by MI compromises both stem cell survival and differentiation [2,3]. This includes low nutrient and oxygen conditions, high concentrations of reactive oxygen species and inflammatory molecules in the infarcted hearts [2,3].

Collagen, a major extracellular matrix (ECM) in the scar tissue, may also contribute to low cell differentiation, although this has not yet been explored in the literature. Following MI, the composition, biomechanics and structure of collagen fibers change continuously [12–23]. Their stiffness gradually increases to 3–4 times that of collagen in healthy heart tissue [24]. A hypothesis is that such increases may affect stem cell differentiation, consistent with recent in vitro studies showing that matrix stiffness regulates stem cell differentiation [25–33]. This hypothesis can be examined by studying how collagen at different stages of MI affects stem cell differentiation.

Recent studies in stem cell biology show that stem cells can differentiate into different lineages in vitro when exposed to intrinsic properties of the matrix, such as composition, biomechanics and structure [34]. These parameters modulate the forces exerted between the cells and matrix. Mechanosensitive pathways subsequently convert these forces into biochemical signals that commit the cell to a specific lineage [34]. Each of these attributes is significant. Matrix composition can regulate cell fate by differential integrin binding to the matrix [34]. For example, ECM proteins can interact with a specific subset of integrins on the mesenchymal stem cell (MSC) surface, directing differentiation into heart cells [35]. Specific domains from ECM proteins can dramatically affect cell differentiation by conformational changes that enhance force transmission as integrins bind to these ligands [36–39]. Matrix structure can also affect stem cell differentiation, by affecting integrin binding and the distribution of focal contacts between the matrix and cells [34]. For example, embryonic stem cells show different differentiation behavior in a microporous foam with solid walls compared to fibrous ones [34,40,41]. Finally, matrix mechanical properties can induce stem cell differentiation. Specifically, stem cells show lineage-specific

differentiation when cultured on matrices mimicking the stiffness of native tissue [25–33]. MSCs become neurogenic, myogenic and osteogenic on matrices mimicking neural, skeletal muscle and bone stiffness environments, respectively [25]. We have demonstrated that MSCs differentiate into cardiomyocytes in a hydrogel with 45–65 kPa modulus [32], while cardiosphere-derived cells (CDCs) differentiate into cardiomyocytes at 35 kPa modulus [31]. More recently, we demonstrated that fibrous scaffolds mimicking the global mechanical properties of healthy heart tissue can induce MSC differentiation into cardiomyocytes [30].

Although many studies have investigated the relationship among collagen global biomechanics, collagen organization and heart function [12–23], the current literature lacks systematic studies of the effect of collagen fibers in scar tissue on stem cell differentiation. Specifically, how do collagen composition, single-fiber modulus, fiber density and alignment evolve at different stages of MI and how do these changes affect cell differentiation? After being delivered into the scar tissue, stem cells adhere to collagen fibers. Fiber properties such as composition, single-fiber modulus, fiber density and alignment determine the forces that a stem cell can exert on collagen fibers. Cells contact single fibers and thus sense the single fiber rather than global modulus. Fiber density and alignment determine the distribution of focal contacts between fibers and cells. The evolution in collagen composition, biomechanics and structure due to MI introduces the possibility that differentiation might be stimulated or inhibited during certain stages. This may impact both the optimal timing for stem cell delivery into infarcted hearts and the design of matrices to promote cardiac differentiation. However, these studies cannot be conducted in vivo, as other parameters such as cytokines and glycosaminoglycans (GAGs) may concurrently affect cell differentiation, making it difficult to isolate the effects of collagen fibers [2,3].

Towards the goal of elucidating the relationship between stem cell differentiation and changes in collagen fiber properties after MI, we created a novel in vitro model based on fibrous scaffolds that mimic structure of the collagen matrix. By modulating fiber composition and fabrication parameters, scaffolds with different single-fiber moduli, global moduli, alignment and fiber density were obtained. CDC cardiac differentiation in the scaffolds was then investigated and correlated to these properties.

2. Materials and methods

2.1. Materials

N-Isopropylacrylamide (NIPAAM, TCI) was recrystallized with hexane three times before use. 2-Hydroxyethyl methacrylate (HEMA, Alfa Aesar) and acrylic acid (AAc, Acros) were purified by passing through an inhibitor-remover column. Polycaprolactone (PCL) diol (Mn = 2000, Acros) was dried under vacuum at 55 °C overnight before use. β-butyrolactone (VWR), gelatin type A (Acros), hexafluoroisopropanol (HFIP, Oakwood), tin(II) trifluoromethanesulfonate ($Sn(OTf)_2$, VWR), 1,6-diisocyanatohexane (HMDI, Acros), 1,4-diaminobutane (DAB, Acros), stannous octoate ($Sn(Oct)_2$, Pfaltz & Bauer) and dimethyl sulfoxide (DMSO, Fisher) were used as received.

2.2. Poly(ester urethane) urea synthesis

Poly(ester urethane) urea (PU) was synthesized from PCL, HMDI and DAB according to our previously established method [42]. In brief, 12.37 g of PCL was dissolved in 150 ml DMSO in a three-necked flask with nitrogen protection. Following addition of 2 ml HMDI and six drops of $Sn(Oct)_2$, the mixture was heated to 70 °C to start the reaction. After 3 h, the solution was cooled to room temperature. A solution of DAB (0.544 g) in 100 ml DMSO was then added dropwise to the flask. The reaction was conducted overnight under stirring. The resulting PU solution was precipitated in excess cool deionized (DI) water and dried under vacuum. The synthesized PU has a glass transition temperature (T_g) of −46 °C, tensile stress of 4.7 ± 0.6 MPa, breaking strain of 946 ± 78%, and Young's modulus of 2.2 ± 0.3 MPa.

2.3. Hydrogel synthesis

The hydrogel was based on NIPAAM, AAc, and a macromer based on HEMA and oligo (β-butyrolactone). The macromer was synthesized by reacting HEMA with β-butyrolactone (molar ratio 1:6) under 110 °C with nitrogen protection for 1 h. $Sn(OTf)_2$ was used as a catalyst. After the reaction, the mixture was cooled to room temperature, dissolved in THF, and precipitated in cool DI water. The precipitate was then dissolved in ethyl acetate, dried over anhydrous magnesium sulfate and filtered. The solvent was removed under reduced pressure. The resulting macromer was abbreviated as HEMA-oHB6.

The hydrogel was synthesized by free radical polymerization using benzoyl peroxide (BPO) as the initiator [43,44]. The molar ratio of NIPAAM/AAc/HEMA-oHB6 was 86/4/10. Stoichiometric amounts of NIPAM, AAc and HEMA-oHB6 were dissolved in dioxane in a three-necked flask. The monomer concentration was controlled at ~5 wt.%. The solution was bubbled with nitrogen for 15 min before BPO solution (in dioxane) was injected into the flask. After 24 h of reaction at 70 °C, the solution was cooled to room temperature and precipitated with hexane. The polymer was purified twice using THF/diethyl ether. The resulting polymer was finally dried under vacuum overnight.

The synthesized hydrogel had a sol–gel temperature of ~14 °C as determined by differential scanning calorimetry (DSC). This allows the hydrogel to maintain a solid state at body temperature. The degradation product poly (NIPAM-co-AAc-co-HEMA) has 4% AAc, which has been demonstrated to have a lower critical solution temperature (LCST) above 37 °C [45]. Therefore, the degraded polymer can be dissolved in body fluid and removed from the body. The hydrogel was highly flexible with a breaking strain >300% and Young's modulus of 11.1 ± 3.5 kPa.

2.4. Mouse cardiosphere-derived cells culture

Mouse CDCs were isolated from the explant of exocardium biopsies as described previously [46]. The CDCs were cultured in Iscove's Modified Eagle Medium (IMDM, Invitrogen) supplemented with 10% fetal bovine serum (FBS, Atlanta Biologicals) and 1% penicillin–streptomycin (Invitrogen) under normal culture conditions (21% O_2, 5% CO_2). Cells at passage 13–17 were used. Previous work has demonstrated that CDCs at these passages preserved phenotype and multipotency [47].

2.5. Effect of electrospraying on CDC survival and growth

To investigate the effect of electrospraying voltage on CDC survival and growth, CDCs were electrosprayed under 10, 15 and 20 kV. Before electrospraying, cells were suspended in culture medium containing 2% gelatin A. Some of the electrosprayed CDCs were then stained with Trypan Blue to determine the percentage of cells that survived during electrospraying. The remaining cells were seeded in a 96-well culture plate to determine if electrospraying affected cell growth. CDCs without electrical treatment were used as the control. After 1, 3 and 5 days of culture, a MTT assay was used to determine cell viability [48].

2.6. Fabrication of tissue constructs by electrospinning and electrospraying

A two-stream electrospinning and electrospraying setup was employed to generate fibrous tissue constructs as described previously [30]. CDCs were suspended in IMDM with 2% gelatin, then loaded into a syringe and charged at +10 kV. Gelatin not only increases the viscosity of the cell suspension for electrospraying, but it also preserves the viability of CDCs during electrospraying [30]. The total number of CDCs used for each tissue construct was 100 million. The cell suspension was injected at a fixed rate of 15 ml h^{-1}. The electrospinning stream included a solution of hydrogel and polyurethane blend (15%, w/v in HFIP). The hydrogel/polyurethane ratio was controlled at 90/10, 70/30 and 50/50 wt.%, respectively. The solution was charged at +15 kV and two different flow rates (4.5 and 7.5 ml h^{-1}) were used. The fibers and CDCs were collected on a rotating mandrel (diameter 11.5 cm, rotation speed 1000 rpm) charged at −10 kV. After ~40 min of fabrication, the tissue constructs were immersed in culture medium overnight. The nomenclature for the resulting constructs is shown in Table 1.

2.7. In vitro culture of tissue constructs

After incubating in culture medium overnight, part of the fabricated construct was cut for dsDNA analysis, cell staining, imaging and mechanical testing. The rest was transferred into a spinner flask for further culture. Each spinner flask was supplemented with 100 ml of culture medium. The samples were harvested after 3 and 7 days of culture for dsDNA analysis, RNA extraction and immunohistochemistry studies.

2.8. CDC survival and growth in tissue constructs

To determine cell distribution in the constructs after fabrication and in vitro culture, the samples were stained with phalloidin rhodamine for F-actin after 1 and 7 days of culture. Confocal images were taken using a Olympus Fluoview 1000 laser scanning confocal microscope.

dsDNA assays were employed to determine the number of living cells in tissue constructs. In brief, tissue constructs collected at each time point were washed with fresh PBS and digested with papain solution overnight at 60 °C [44]. PicoGreen (Invitrogen) was then added to the digested solution followed by fluorescent intensity measurements using a fluorescence plate reader at an excitation wavelength of 480 nm and emission wavelength of 520 nm. Standard dsDNA with graded concentrations was used to calibrate the fluorescence

intensity vs. DNA concentration. The dsDNA content for each construct was normalized by the weight of the construct.

2.9. Construct characterization

Tissue construct morphology was determined using scanning electron microscopy (SEM). The samples were prepared following previous reports [49–51]. Briefly, the constructs were fixed with 4% paraformaldehyde at 37 °C for 1 h. After rinsing with PBS, the constructs were dehydrated by 50%, 70%, 80%, 95% and 100% ethanol solutions in sequence. Hexamethyldisilazane was then used to chemically dry the samples. To image the interior structure, the surface layer of the constructs was peeled off. To image the construct cross-section, the constructs were frozen in liquid nitrogen and quickly cut by a blade. The samples were finally sputter-coated with gold and imaged with a FEI NOVA nanoSEM. Fiber diameters were determined from SEM images of the interior structure using Image J software, while fiber densities were calculated from SEM images of tissue construct cross-sections. Fiber orientation distributions within the tissue constructs were calculated by using a Hough transformation algorithm in Matlab, based on the SEM images of the scaffolds.

Single-fiber modulus was measured by a BioScope Catalyst atomic force microscope (Bruker Corporation) equipped with a water bath. The testing was conducted in PBS at 37 °C. The samples were scanned with a Tap 150A probe. The tip parameters are as follows: $k = 5\ \mathrm{N\ m^{-1}}$, nominal tip radius = 8 nm, Poisson's ratio = 0.5. After visualizing and identifying single polymer fibers, mapping of the mechanical properties on single fibers was performed under PeakForce Quantitative Nanomechanical (QNM) imaging (Standard Amplitude) mode. For each group, 2–3 samples were measured and 4–6 locations were scanned. The scan area at each location was about $50 \times 50\ \mu m^2$, and the scanning rate was 0.5 Hz. For the modulus measurement, a ramp size of 2 μm (Deflection Mode, Relative; Threshold, 30 nm) was taken at each data point. A minimum of 500 data points (force–displacement curves on individual fibers) was obtained at each location. The data were then analyzed using NanoScope Analysis software (Bruker Corporation).

The mechanical properties of the tissue constructs with and without cells were assessed by uniaxial tensile testing. The testing was performed on a TestResources 1000R load frame (model 1322) equipped with a 50 lb load cell and a 37 °C water bath. A cross-head speed of $10\ \mathrm{mm\ min^{-1}}$ was employed. At least eight 20 mm × 2.5 mm size samples were tested for each construct.

The resulting uniaxial tensile mechanical response of the tissue constructs was related to the hydrogel/polyurethane fiber angular distribution following the constitutive development of Sacks et al. [52,53]. Here, it is assumed that a representative volume element (RVE) can be identified to capture the microstructure in average sense. The RVE is treated as a three-dimensional continuum and assumed to be small relative to the macroscopic scale of the constructs. The hydrogel/polyurethane fibers are modeled as a hyperelastic solid. Within the RVE, the following assumptions are made:

1. The tissue is idealized as a planar fiber network, and the hydrostatic effect from surrounding water is not modeled.

2. The undulation of the hydrogel/polyurethane fibers is assumed to gradually disappear with stretching on the scaffold. The load required to straighten the fibers is negligible compared to the load transmitted once the stretched fibers are straightened.
3. The fiber strain can be calculated from the transformation of the global strain tensor to the local fiber basis.
4. The strain energy function of the constructs is the sum of the individual fiber strain energies.
5. The mechanical contribution of cells is not explicitly modeled.

From assumption 3, the uniaxial strain ε along each fiber is expressed in terms of the global tissue strain tensor **E** and fiber axis direction **N**:

$$\varepsilon = \mathbf{N}^T \cdot \mathbf{E} \cdot \mathbf{N}, \text{where } N_1 = \cos\theta,\ N_2 = \sin\theta,\ N_3 = 0 \quad (1)$$

Thus, θ is the angle subtended by the fiber axis and the tensile direction (1-axis), which is parallel to the circumferential direction of the mandrel during fiber spinning. Assumption 1 imposes $N_3 = 0$.

From assumption 4, the strain energy per unit volume of scaffold is:

$$W = V_f \int_{-\pi/2}^{\pi/2} R(\theta) w(\varepsilon)\, d\theta\,. \quad (2)$$

Here, w is the strain energy per unit volume of fiber, $R(\theta)$ is the distribution of fiber orientations, and V_f is the volume fraction of fibers in the RVE. The second Piola–Kirchoff stress S along the 1 (tensile) axis and the corresponding local stress σ along the fiber axis are:

$$S = \frac{\partial W}{\partial \mathbf{E}} \text{ and } \sigma = \frac{\partial w}{\partial \varepsilon} \quad (3)$$

Here, E is the Green–Lagrange strain in the RVE along the tensile axis. Using Eqs. (1–3) furnishes a tensile stress–strain relationship for the RVE [54]:

$$S = V_f \int_{-\pi/2}^{\pi/2} R(\theta)\, \sigma(\varepsilon)[cos^2\theta - \nu sin^2\theta]\, d\theta\,. \quad (4)$$

The bracketed term [ ] = $d\varepsilon/dE$, where Poisson's ratio of the RVE is defined by $\nu = -E_T/E$, the ratio of the transverse and axial strains during a tension test.

Expressions for the elastic modulus of the scaffold at small and large strain can be developed from Eq. (4). The fiber orientation distribution function $R(\theta)$ can be determined by a fit based on a modified Cauchy distribution:

$$R(\theta) = \frac{a}{\pi} + \frac{1-a}{\pi c[1+(\theta - L)^2/c^2]}, \quad (5)$$

where a represents the random orientation component, c is a shape parameter, and the location parameter $L = 0$ since the samples are aligned to the scaffold axis. In the small strain regime, the elastic modulus of the fiber is described by a relatively small value m_0, valid during the initial stages of stretch before the fibers become straight. If $\sigma = m_0 \varepsilon$ is inserted into Eq. (4), the elastic modulus M_0 of the RVE at small strain is:

$$M_0 = V_f m_0 A_0, \quad A_0 = \int_{-\pi/2}^{\pi/2} R_0(\theta)[cos^2\theta - vsin^2\theta]^2 d\theta. \quad (6)$$

In the opposing limit when the applied strain is sufficiently large to fully straighten the fibers, the incremental modulus of the fibers is assumed to have a larger value m_L. In this limit, the fibers are assumed to be fully aligned at $\theta = 0$, so that $A = 1$ and the RVE modulus at large strain is:

$$M_L = V_f m_L. \quad (7)$$

2.10. CDC cardiac differentiation in tissue constructs

CDC differentiation in tissue constructs was determined by real-time reverse transcription polymerase chain reaction (RT-PCR) and immunohistochemistry. Cells cultured on tissue culture plate (TCP) were used as a control. Tissue constructs were collected after 3 or 7 days of culture in spinner flasks. RNA was extracted from the constructs by TRIzol (Sigma). Approximately 1 μg of RNA was used to synthesize cDNA using High Capacity cDNA Reverse Transcription Kits (Applied Biosystem). Real-time RT-PCR was performed with a Mastercycler ep gradient S thermal cycler (Eppendorf) and Platinum *Taq* DNA Polymerase (Life Tech.) with primers listed in Table 2. Fold differences were calculated using the standard ΔΔCt method with β-actin as the housekeeping gene [55,56].

For immunohistochemical analysis, the tissue constructs were fixed with 4% paraformaldehyde at 37 °C for 1 h. After rinsing with fresh PBS, the constructs were frozen with OCT and sectioned into 10 μm thick slices. The slices were then blocked with 10% goat serum in 0.1% Triton X-100 for 1 h, followed by incubation with mouse monoclonal anti-cTnI and anti-CX43 (Abcam) antibodies respectively at 37 °C overnight. Both cTnI and CX43 are expressed in mature cardiomyocytes. After rinsing with PBS, the corresponding secondary antibodies were added and incubated for another 1 h. Slices without primary antibody but with secondary antibody treatment were used as a negative control. The slices

were finally stained with Hoechst 33342 for nuclei. Images were taken with an Olympus FV1000 filter confocal microscope.

A functional response parameter GP was calculated based on the gene and protein expression to quantitatively indicate the cell differentiation. The specific gene and protein expressions were normalized first based on the results of real time RT-PCR and immunohistochemical analysis, respectively. The protein expression was quantified as the fraction of cells positive to a given protein. Then the overall gene expression G and protein expression P were calculated by $G = \Sigma G_{NG}/N_G$ and $P = \Sigma P_{NP}/N_P$, respectively, where N_G and N_P are the number of genes and proteins, respectively. The GP value was then determined by multiplying the normalized G and P values.

2.11. CDC adhesion on hydrogel/polyurethane blends

CDCs were seeded on hydrogel/polyurethane film to evaluate cell adhesion capacity. Three blends with different hydrogel/polyurethane ratios (90/10, 70/30 and 50/50) were used. The hydrogel/polyurethane blends were cut into 6 mm discs and fitted into 96-well plates. Each well was seeded with 2×10^5 cells. After 24 h of culture, the culture medium was removed and samples were washed three times with DPBS. Cells cultured on TCP were used as control. The dsDNA content was tested as described above.

2.12. Statistical methods

Data are expressed as mean ± standard deviation. Statistical comparisons were performed by ANOVA using JMP. Significant difference is defined as $p < 0.05$.

3. Results

3.1. Effect of electrospraying voltage on CDC survival and growth

CDCs were electrosprayed at different voltages to investigate the effect of electric field on cell survival and growth. Table 3 shows that >97% of the electrosprayed cells survived under 10, 15, and 20 kV. There was no significant difference in the cell survival rate between the control and electrosprayed groups. The electrosprayed cells were able to proliferate during the culture with similar growth kinetics to cells that were not electrosprayed (Fig. 1).

3.2. Fabrication and characterization of tissue constructs

Tissue constructs with a high density of CDCs were successfully fabricated using a technique involving simultaneous fiber electrospinning and cell electrospraying. The electrosprayed CDCs and electrospun fibers were homogeneously distributed in the constructs (Figs. 2 and 3). The fibers assumed diameters typically >1 μm with no significant difference between different constructs (Table 4). The fiber density and alignment were dependent on the pumping speed of polymer solution (Table 4). An increase in pumping speed from 4.5 to 7.5 ml h^{-1} significantly increased fiber density ($n = 10$, $p < 0.05$) but decreased fiber alignment ($p < 0.05$).

Fiber alignment was calculated by Matlab based on the SEM images using Eq. (6).

Typical stress–strain curves of the four tissue constructs with cells are presented in Fig. 4 and the tensile properties are summarized in Table 5. The constructs were highly flexible and relatively strong with tensile strains and strengths greater than 362% and 440 kPa, respectively. The constructs were also relatively soft with small strain tensile moduli M_0 ranging from 4.8×10^1 to 4.6×10^2 kPa. The tensile modulus and strength were dependent on the PU/hydrogel ratio and polymer solution pumping speed. Table 5 demonstrates that an increase in PU/hydrogel ratio significantly increased tensile strength and modulus ($n = 8$, $p < 0.05$). At the same PU/hydrogel ratio, increasing the polymer solution pumping speed from 4.5 to 7.5 ml h^{-1} increased the tensile strength ($n = 8$, $p < 0.05$) but not modulus ($n = 8$, $p > 0.05$).

The small strain tensile moduli of the constructs without cells on days 1 and 7 are presented in Table 6. The tensile modulus of the constructs without cells was not significantly different from that with cells. Also, the tensile modulus of the constructs without cells did not change significantly after 7 days of incubation ($n = 6$, $p > 0.1$), indicating that no obvious degradation occurred during this period.

The modulus of the single fibers in tissue constructs was measured by atomic force microscopy (AFM) in a 37 °C water bath. These AFM-based moduli are denoted m_A and ranged from 130 kPa to 1 MPa. They depended on the PU/hydrogel ratio but not pumping speed (Fig. 5). In general, fibers with a higher PU/hydrogel ratio assumed a greater modulus ($n > 4000$, $p < 0.05$).

3.3. CDC adhesion on hydrogel/PU blends and cell survival in tissue constructs

To investigate if fiber composition had an effect on CDC attachment, the cells were seeded on 2-D films of PU/hydrogel blends with different ratios and cell adhesion was characterized after 24 h of culture. Fig. 6 shows that there was no significant difference among all three films with different PU/hydrogel ratios ($n = 6$, $p < 0.05$), demonstrating that the PU/hydrogel ratio did not affect CDC adhesion. Interestingly, the cell adhesion on PU/hydrogel films was much greater than that on the tissue culture plate.

The fabricated tissue constructs were ~150 μm thick. The use of a spinner flask enhanced the oxygen and nutrient transport in the constructs during the culture. Fig. 7 demonstrates that CDCs survived in the constructs during the 7 day culture period. Comparison of the dsDNA content in each tissue construct after 1 and 7 days of culture showed no significant difference between the two time points ($n = 6$, $p > 0.05$, Fig. 7).

3.4. Cardiac differentiation of CDCs in tissue constructs

The cardiac differentiation of CDCs in tissue constructs was evaluated at the mRNA level by real-time RT-PCR, and at the protein level by immunohistochemistry. At the mRNA level, cardiac specific markers cardiac troponin T (cTnT), cardiac myosin heavy chain alpha (MYH6) and calcium channel protein (CACNA1c) were used to assess the degree of CDC cardiac differentiation. As seen in Fig. 8, these markers were all significantly up-regulated in constructs (A) and (B). Meanwhile, almost no mature cardiac markers were expressed in the other two constructs. Overall construct (A) exhibited the highest expressions. At the protein level, CDCs in constructs (A) and (B) were both cTnI and CX43 positive (Figs. 9 and 10).

However, the cells in constructs (C) and (D) were cTnI negative and showed weak expression of CX43. These results demonstrate that construct (A) most significantly stimulated CDC cardiac differentiation.

4. Discussion

The purpose of this work was to determine the optimal physical properties of fibrous tissue constructs that lead to cardiac differentiation of CDCs. This work represents the first step towards elucidating the relationship between stem cell cardiac differentiation and changes in collagen fiber properties after MI. Various studies have demonstrated that matrix properties such as composition, biomechanics and structure affect stem cell differentiation [25,57–61]. However, most of these studies were conducted either in a 2-D environment or in nonfibrous scaffolds. These studies therefore cannot elucidate stem cell differentiation in the 3-D fibrous scaffolds that resemble the morphology and structure of the native ECM. For fibrous scaffolds, physical properties such as composition, modulus, fiber diameter and alignment potentially affect cell differentiation, as they affect mechanopathways and the focal adhesion of cells [25,57–61]. However, no previous work has investigated the effect of these properties on CDC cardiac differentiation. In this work, we found that when fibers with the same cell adhesive properties were used, CDC cardiac differentiation was determined by the scaffold macroscopic tensile modulus at small strain (M_0), fiber volume fraction V_f and fiber alignment A_0.

4.1. Geometric and mechanical properties of tissue constructs

Key trends among the processing, geometric and mechanical parameters are observed among the summary results presented in Table 7. Tissue constructs were fabricated through simultaneous electrospinning of polymer fibers and electrospraying of cells. Here, pumping speed P and hydrogel content H were varied. The use of both compliant hydrogel (~10 kPa) and relatively stiff PU (~2.2 MPa) enabled constructs with heart tissue-like mechanical properties. In particular, the small strain tensile moduli of the constructs ranged from M_0 = 48 to 461 kPa. This is within the modulus range of the native heart tissue during a beating cycle (10–500 kPa) [62].

The trends in fiber volume fraction V_f and fiber alignment A_0 at small strain show peculiar differences for construct (A) compared to the others. Here, $V_f = n\,\pi d^2/4$ is used, where n and d are reported in Table 4. The large V_f for construct (A) stems from a considerably larger n and modestly larger d (Table 4). Apparently, the larger pump speed generates greater packing of fibers. The fiber alignment function A_0 is also smaller, indicating a broader fiber distribution about the perfectly aligned ($\theta = 0$) case. This is consistent with a larger pump speed, which increases the speed of the impinging polymer stream relative to the fixed mandrel speed. For case (A), the speed of the impinging polymer stream is estimated as $s_p \approx P/A_{nozzle} = 2.19\ m\ s^{-1}$ and the circumferential speed on the mandrel of diameter D_m and revolutions per second w is estimated as $s_m \approx w\pi D_m = 0.785\ m\ s^{-1}$. The SEM images in Fig. 3 confirm the larger V_f and smaller A_0 for construct (A), compared to construct (B). Comparison of cases (B)–(D) shows that alignment and volume fraction are controlled primarily by pump speed rather than by hydrogel fraction. This is surprising since the results

(to follow) show a large variation in fiber modulus, which could in principle affect V_f and A_0.

These geometric and processing features translate into a range of macroscopic moduli at both small strain (M_0) and large strain (M_L). Constructs (A) and (B) have comparable values of M_0 that are ~25% or less than for cases (C) and (D). The comparable values demonstrate that M_0 can be held relatively constant by increasing pump speed at constant hydrogel fraction, thereby increasing V_f while decreasing A_0. M_L is larger in case (A) vs. (B), which is consistent with a larger V_f. Overall, however, the large increase in V_f produces rather modest gains in M_L. Comparison of cases (C) and (D) shows that increases in both the small and large strain moduli are achieved by decreasing the hydrogel fraction.

The data also address how the local fiber moduli at small and large strain depend on pump speed and hydrogel fraction. The fiber moduli m_A (Fig. 5) from AFM can be complemented by estimates of m_0 and m_L using Eqs. (6) and (7). In particular, the small strain fiber moduli m_0 are obtained by inserting experimental values of V_f, A_0 and M_0 into Eq. (6), and the large strain counterpart m_L is obtained by inserting V_f and M_L into Eq. (7). All three fiber moduli (m_A, m_0, m_L) increase as the PU fraction increases (H decreases). Changing the pump speed produces no significant difference ($n > 4000$, $p > 0.05$) in fiber modulus. The results indicate that m_0 is ~80% of m_L, consistent with the effects of increased polymer chain alignment and overall fiber straightening at larger strain.

A relevant experimental issue is the most efficacious approach to estimate fiber modulus. AFM is desirable both because it is not inferred indirectly through formulae (Eqs. (6) and (7)) that require measurements or assumptions about fiber alignment. However, drawbacks to AFM include the inhomogeneous stress state generated under the tip, support of the fiber, and elastic anisotropy in the radial vs. axial directions of the fiber. Drawbacks to Eqs. (6) and (7) include the effect of cells on the measurement of M_0 and M_L. These effects were neglected in Eqs. (6) and (7) so that the resulting values of m_0 and m_L are expected to be upper bounds. Despite the drawbacks to each method, it is encouraging that they yielded consistent trends with pump speed and hydrogel fraction.

4.2. Cardiac differentiation

The differentiation of CDCs towards cardiac linage was evidenced by real-time RT-PCR (Fig. 8) and immunohistochemistry (Figs. 9 and 10). At the mRNA level, cardiac differentiation was dependent on the tissue construct modulus, fiber diameter and fiber density. Overall, CDCs in the construct with the lowest modulus (M_0 = 48 kPa) and the highest fiber volume fraction (V_f = 0.85) demonstrated the highest expressions of mature cardiac markers cTnT, MYH6 and CACNA1c. Statistical analysis showed that M_0 had a significant effect on the expressions of MYH6 and CACNA1c. Interestingly, V_f played an important role in the cTnI expression where a larger V_f led to a higher extent of expression. At the protein level, CDCs in both M_0 = 48 and 60 kPa constructs were positive to cTnI, but not in the 220 and 460 kPa constructs. Almost all constructs exhibited CX43 expression, though cells in the 48 and 60 kPa constructs had remarkably higher expression than those in the 220 and 460 kPa constructs.

Matrix modulus has been shown to affect cell differentiation. In the current study, the constructs (B), (C) and (D) had very similar fiber diameter d, density n and alignment A_0 ($p > 0.05$) but different scaffold modulus. The gene and protein expression results demonstrate that the optimal modulus for CDC cardiac differentiation in fibrous scaffolds is ~50 kPa. This value is slightly higher than that of CDC cardiac differentiation in 3-D hydrogels. As reported in our previous study, the optimal modulus for CDC cardiac differentiation in PNIPAAm-based hydrogels is 31–40 kPa [31,63]. The discrepancy may result from different microenvironments in the hydrogel and fibrous scaffold.

Fig. 11 shows the results of a statistical analysis of the gene and protein expressions, leading to a fit of the functional performance:

$$GP = (B \times V_f) \times exp[K(M_0 - C)^2 + D]. \quad (8)$$

The fitted function captures the experimental points well ($R^2 = 0.98$, $p < 0.05$, $p < 0.0001$, $p < 0.0001$ for V_f, M_0 and M_0^2, respectively). Over the scaffold modulus range $M_0 = 50–500$ kPa, the lower values produced higher cardiac differentiation of the seeded CDCs. It is unclear whether even smaller M_0 might yield further increases in GP.

The results for cases (A) and (B) in Table 7 show that GP depends on more than fiber and construct moduli. In particular, cases (A) and (B) have similar M_0 ($p > 0.05$)and m ($p > 0.05$) for m_0, m_L and m_A from AFM tests). Yet GP for (A) is ~7 times that for (B). This may be attributed to the larger V_f and smaller fiber alignment A_0. This is confirmed in Fig. 8, based on the larger fiber density in the cross-sectional views and reduced fiber alignment in the side views, for (A) compared to (B). A positive coefficient B in Eq. (8) also indicates that a higher fiber volume fraction increases GP. This was achieved primarily by increasing the fiber density. In principle, V_f can also be increased with a larger fiber diameter but the effect on GP is not known from the present work. The effect of fiber density and alignment on cell differentiation may result from their effects on the number of cell adhesion sites, focal adhesion shape, cell–cell distance and cell shape. Various studies have demonstrated that these parameters determine cell differentiation [60–62,64].

5. Conclusions

In this work, ECM-like fibrous tissue constructs with different global modulus, single-fiber modulus, fiber density and alignment were fabricated to investigate the effect of construct properties on CDC cardiac differentiation. Constructs with a small strain global modulus of 48 kPa, a larger fiber volume fraction of ~ 0.9, and lower alignment ($A_0 = 0.45$) were found to stimulate cardiac differentiation most effectively. This study suggests that ECM properties in heart tissue will have an impact on cardiac differentiation of delivered stem cells, and the timing of stem cell delivery may affect the extent of cardiac differentiation.

Acknowledgments

The assistance of Dr. John Lannutti's group (OSU) with mechanical testing and Dr. Andrew Fischer's group (OSU) with real-time RT-PCR testing is greatly appreciated. This work was supported by National Science Foundation (1160122 and 1006734), the American Heart Association (13GRNT17150041), and a Multidisciplinary Research Group seed grant from the Institute of Materials Research at The Ohio State University.

References

1. American Heart Association. Heart Disease and Stroke Statistics—2012 Update. Dallas, TX: American Heart Association; 2012.
2. Laflamme MA, Murry CE. Heart regeneration. Nature. 2011; 473:326–35. [PubMed: 21593865]
3. Wang F, Guan J. Cellular cardiomyoplasty and cardiac tissue engineering for myocardial therapy. Adv Drug Deliv Rev. 2010; 62:784–97. [PubMed: 20214939]
4. Herrmann JL, Abarbanell AM, Weil BR, Wang Y, Wang M, Tan J, et al. Cell-based therapy for ischemic heart disease: a clinical update. Ann Thorac Surg. 2009; 88(5):1714–22. [PubMed: 19853156]
5. Forrester JS, Makkar RR, Marbán E. Long-term outcome of stem cell therapy for acute myocardial infarction: right results, wrong reasons. J Am Coll Cardiol. 2009; 53:2270–2. [PubMed: 19520250]
6. Jameel MN, Zhang J. Heart failure management: the present and the future. Antioxid Redox Signal. 2009; 11(8):1989–2010. [PubMed: 19203220]
7. Quevedo HC, Hatzistergos KE, Oskouei BN, Feigenbaum GS, Rodriguez JE, Valdes D, et al. Allogeneic mesenchymal stem cells restore cardiac function in chronic ischemic cardiomyopathy via trilineage differentiating capacity. Proc Natl Acad Sci U S A. 2009; 106:14022–7. [PubMed: 19666564]
8. Malliaras K, Marbán E. Cardiac cell therapy: where we've been, where we are, and where we should be headed. Br Med Bull. 2011; 98:161–85. [PubMed: 21652595]
9. Nguyen PK, Nag D, Wu JC. Methods to assess stem cell lineage, fate and function. Adv Drug Deliv Rev. 2010; 62(12):1175–86. [PubMed: 20816906]
10. Bursac N. Cardiac tissue engineering using stem cells. IEEE Eng Med Biol Mag. 2009; 28:88–9.
11. Vunjak-Novakovic G, Tandon N, Godier A, Maidhof R, Marsano A, Martens TP, et al. Challenges in cardiac tissue engineering. Tissue Eng Part B Rev. 2010; 16(2):169–87. [PubMed: 19698068]
12. Fomovsky GM, Macadangdang JR, Ailawadi G, Holmes JW. Model-based design of mechanical therapies for myocardial infarction. J Cardiovasc Transl Res. 2011; 4(1):82–91. [PubMed: 21088945]
13. Fomovsky GM, Holmes JW. Evolution of scar structure, mechanics, and ventricular function after myocardial infarction in the rat. Am J Physiol Heart Circ Physiol. 2010; 298(1):H221–8. [PubMed: 19897714]
14. Campbell PH, Hunt DL, Jones Y, Harwood F, Amiel D, Omens JH, McCulloch AD. Effects of biglycan deficiency on myocardial infarct structure and mechanics. Mol Cell Biomech. 2008; 5(1): 27–35. [PubMed: 18524244]
15. Herrmann KL, McCulloch AD, Omens JH. Glycated collagen cross-linking alters cardiac mechanics in volume-overload hypertrophy. Am J Physiol Heart Circ Physiol. 2003; 284(4):H1277–84. [PubMed: 12595292]
16. Weis SM, Emery JL, Becker KD, McBride DJ Jr, Omens JH, McCulloch AD. Myocardial mechanics and collagen structure in the osteogenesis imperfecta murine (oim). Circ Res. 2000; 87(8):663–9. [PubMed: 11029401]
17. Holmes JW, Borg TK, Covell JW. Structure and mechanics of healing myocardial infarcts. Annu Rev Biomed Eng. 2005; 7:223–53. [PubMed: 16004571]
18. Gupta KB, Ratcliffe MB, Fallert MA, Edmunds LH Jr, Bogen DK. Changes in passive mechanical stiffness of myocardial tissue with aneurysm formation. Circulation. 1994; 89:2315–26. [PubMed: 8181158]
19. Holmes JW, Covell JW. Collagen fiber orientation in myocardial scar tissue. Cardiovasc Pathobiol. 1996; 1:15–22.

20. Holmes JW, Nunez JA, Covell JW. Functional implications of myocardial scar structure. Am J Physiol Heart Circ Physiol. 1997; 272:H2123–30.
21. Connelly CM, Vogel WM, Wiegner AW, Osmers EL, Bing OH, Kloner RA, et al. Effects of reperfusion after coronary artery occlusion on post-infarction scar tissue. Circ Res. 1985; 57:562–77. [PubMed: 4042284]
22. Whittaker P, Boughner DR, Kloner RA. Analysis of healing after myocardial infarction using polarized light microscopy. Am J Pathol. 1989; 134:879–93. [PubMed: 2705508]
23. Whittaker P, Kloner RA, Boughner DR, Pickering JG. Quantitative assessment of myocardial collagen with picrosirius red staining and circularly polarized light. Basic Res Cardiol. 1994; 89:397–410. [PubMed: 7535519]
24. Berry MF, Engler AJ, Woo YJ, Pirolli TJ, Bish LT, et al. Mesenchymal stem cell injection after myocardial infarction improves myocardial compliance. Am J Physiol Heart Circ Physiol. 2006; 290:H2196–203. [PubMed: 16473959]
25. Engler AJ, Sen S, Sweeney HL, Discher DE. Matrix elasticity directs stem cell lineage specification. Cell. 2006; 126(4):677–89. [PubMed: 16923388]
26. Burdick JA, Vunjak-Novakovic G. Engineered microenvironments for controlled stem cell differentiation. Tissue Eng Part A. 2009; 15:205–19. [PubMed: 18694293]
27. Discher DE, Mooney DJ, Zandstra PW. Growth factors, matrices, and forces combine and control stem cells. Science. 2009; 324:1673–7. [PubMed: 19556500]
28. Winer JP, Janmey PA, McCormick ME, Funaki M. Bone marrow-derived human mesenchymal stem cells become quiescent on soft substrates but remain responsive to chemical or mechanical stimuli. Tissue Eng Part A. 2009; 15:147–54. [PubMed: 18673086]
29. Huebsch N, Arany PR, Mao AS, Shvartsman D, Ali OA, Bencherif SA, et al. Harnessing traction-mediated manipulation of the cell/matrix interface to control stem-cell fate. Nat Mater. 2010; 9:518–26. [PubMed: 20418863]
30. Guan J, Wang F, Li Z, Chen J, Guo X, Liao J, et al. The stimulation of the cardiac differentiation of mesenchymal stem cells in tissue constructs that mimic myocardium structure and biomechanics. Biomaterials. 2011; 32(24):5568–80. [PubMed: 21570113]
31. Li Z, Guo X, Matsushita S, Guan J. Differentiation of cardiosphere-derived cells into a mature cardiac lineage using biodegradable poly(N-isopropylacrylamide) hydrogels. Biomaterials. 2011; 32(12):3220–32. [PubMed: 21296413]
32. Li Z, Guo X, Palmer AF, Das H, Guan J. High-efficiency matrix modulus-induced cardiac differentiation of human mesenchymal stem cells inside a thermosensitive hydrogel. Acta Biomater. 2012; 8(10):3586–95. [PubMed: 22729021]
33. Kraehenbuehl TP, Zammaretti P, der Vlies AJV, Schoenmakers RG, Lutolf MP, Hubbell JA. Three-dimensional extracellular matrix directed cardioprogenitor differentiation: systematic modulation of asynthetic cell-responsive PEG-hydrogel. Biomaterials. 2008; 29:2757–66. [PubMed: 18396331]
34. Reilly GC, Engler AJ. Intrinsic extracellular matrix properties regulate stem cell differentiation. J Biomech. 2010; 43(1):55–62. [PubMed: 19800626]
35. Conrad C, Niess H, Huss R, Huber S, von Luettichau I, Nelson PJ, et al. Multipotent mesenchymal stem cells acquire a lymphendothelial phenotype and enhance lymphatic regeneration in vivo. Circulation. 2009; 119(2):281–9. [PubMed: 19118255]
36. Friedland JC, Lee MH, Boettiger D. Mechanically activated integrin switch controls alpha5beta1 function. Science. 2009; 323:642–4. [PubMed: 19179533]
37. Martino MM, Mochizuki M, Rothenfluh DA, Rempel SA, Hubbell JA, Barker TH. Controlling integrin specificity and stem cell differentiation in 2D and 3D environments through regulation of fibronectin domain stability. Biomaterials. 2009; 30:1089–97. [PubMed: 19027948]
38. Rowlands AS, George PA, Cooper-White JJ. Directing osteogenic and myogenic differentiation of MSCs: interplay of stiffness and adhesive ligand presentation. Am J Physiol Cell Physiol. 2008; 295:C1037–44. [PubMed: 18753317]
39. Yasunaga M, Tada S, Torikai-Nishikawa S, Nakano Y, Okada M, Jakt LM, et al. Induction and monitoring of definitive and visceral endoderm differentiation of mouse ES cells. Nat Biotechnol. 2005; 23:1542–50. [PubMed: 16311587]

40. Ruiz SA, Chen CS. Emergence of patterned stem cell differentiation within multicellular structures. Stem Cells. 2008; 26:2921–7. [PubMed: 18703661]
41. Stevens MM, George JH. Exploring and engineering the cell surface interface. Science. 2005; 310:1135–8. [PubMed: 16293749]
42. Guan J, Sacks MS, Beckman EJ, Wagner WR. Synthesis, characterization, and cytocompatibility of elastomeric, biodegradable poly(ester-urethane)ureas based on poly(caprolactone) and putrescine. J Biomed Mater. 2002; 61:493–503.
43. Wang F, Li Z, Khan M, Tamama K, Kuppusamy P, Wagner WR, et al. Injectable, rapid gelling and highly flexible hydrogel composites as growth factor and cell carriers. Acta Biomater. 2010; 6:1978–91. [PubMed: 20004745]
44. Li Z, Wang F, Roy S, Sen CK, Guan J. Injectable, highly flexible, and thermosensitive hydrogels capable of delivering superoxide dismutase. Biomacromolecules. 2009; 10:3306–16. [PubMed: 19919046]
45. Guan J, Hong Y, Ma Z, Wagner WR. Protein-reactive, thermoresponsive copolymers with high flexibility and biodegradability. Biomacromolecules. 2008; 9:1283–92. [PubMed: 18324775]
46. Davis DR, Zhang Y, Smith RR, Cheng K, Terrovitis J, Malliaras K, et al. Validation of the cardiosphere method to culture cardiac progenitor cells from myocardial tissue. PLoS One. 2009; 4:e7195. [PubMed: 19779618]
47. Ye J, Boyle A, Shih H, Sievers RE, Zhang Y, Prasad M, et al. Sca-1+ cardiosphere-derived cells are enriched for Isl1-expressing cardiac precursors and improve cardiac function after myocardial injury. PLoS One. 2012; 7:e30329. [PubMed: 22272337]
48. De Souza LB, de Aquino SG, de Souza PP, Hebling J, Costa CA. Cytotoxic effects of different concentrations of chlorhexidine. Am J Dent. 2007; 20:400–4. [PubMed: 18269133]
49. Ziv-Polat O, Skaat H, Margel S. Novel magnetic fibrin hydrogel scaffolds containing thrombin and growth factors conjugated iron oxide nanoparticles for tissue engineering. Int J Nanomedicine. 2012; 7:1259–74. [PubMed: 22419873]
50. McBane JE, Vulesevic B, Suuronen EJ. Evalustion of collagen-chitosan hydrogel for potential use as a pro-angiogenic site for islet transplantation. PLoS One. 2013; 8(10):e77538. [PubMed: 24204863]
51. Huang H, Ding Y, Nguyen TA. Peptide hydragelation and cell encapsulation for 3D culture of MCF-7 breast cancer cells. PLoS One. 2013; 8(3):e59482. [PubMed: 23527204]
52. Sacks MS. Incorporation of experimentally-derived fiber orientation into a structural constitutive model for planar collagenous tissues. J Biomed Eng. 2003; 125:280–7.
53. Sacks MS. A structural constitutive model for chemically treated planar tissues under biaxial loading. Comput Mech. 2000; 26:243–9.
54. Gilbert TW, Badylack FB, Chancellor MB, Sacks MS, et al. Fiber kinematics of small intestinal submucosa under biaxial and uniaxial stretch. J Biomech Eng. 2006; 128(6):890–8. [PubMed: 17154691]
55. Davis DR, Zhang Y, Smith RR, Cheng K, Terrovitis J, Malliaras K, et al. Validation of the cardiosphere method to culture cardiac progenitor cells from myocardial tissue. PloS One. 2009; 4:e7195. [PubMed: 19779618]
56. Real-time Quantitative RT-PCR. Design, calculations, and statistics. The Plant Cell. 2009; 21:1031–3. [PubMed: 19395682]
57. Badami AS, Kreke MR, Thompson MS, Riffle JS, Goldstein AS. Effect of fiber diameter on spreading, proliferation, and differentiation of osteoblastic cells on electrospun poly(lactic acid) substrates. Biomaterials. 2006; 27:596. [PubMed: 16023716]
58. Holst J, Watson S, Lord MS, Eamegdool SS, Bax DV, Nivison-Smith LB, et al. Substrate elasticity provides mechanical signals for the expansion of hemopoietic stem and progenitor cells. Nat Biotech. 2010; 28:1123–8.
59. Engelmayr GC, Cheng M, Bettinger CJ, Borenstein JT, Langer R, Freed LE. Accordion-like honeycombs for tissue engineering of cardiac anisotropy. Nature Mater. 2008; 7(12):1003–10. [PubMed: 18978786]

60. McNamara LE, McMurray RJ, Biggs MJP, Kantawong F, Oreffo ROC, Dalby MJ. Nanotopographical control of stem cell differentiation. J Tissue Eng. 2010; 2010:120623. [PubMed: 21350640]

61. Beningo KA, Dembo M, Kaverina I, Small JV, Wang YL. Nascent focal adhesions are responsible for the generation of strong propulsive forces in migrating fibroblasts. J Cell Biol. 2001; 153:881–8. [PubMed: 11352946]

62. Venugopal JR, Prabhakaran MP, Mukherjee S, Ravichandran R, Dan K, Ramakrishna S. Biomaterial strategies for alleviation of myocardial infarction. J R Soc Interface. 2012; 9:1–19. [PubMed: 21900319]

63. Li Z, Guo X, Guan J. An oxygen release system to augment cardiac progenitor cell survival and differentiation under hypoxic condition. Biomaterials. 2012; 33(25):5914–23. [PubMed: 22656447]

64. Guilak F, Cohen DM, Estes BT, Gimble JM, Liedtke W, Chen CS. Control of stem cell fate by physical interactions with the extracellular matrix. Cell Stem Cell. 2009; 5(1):17–26. [PubMed: 19570510]

Appendix A. Figures with essential colour discrimination

Certain figures in this article, particularly Figs. 1–5, 7 and 9–11, are difficult to interpret in black and white. The full colour images can be found in the on-line version, at http://dx.doi.org/10.1016/j.actbio.2014.04.018.

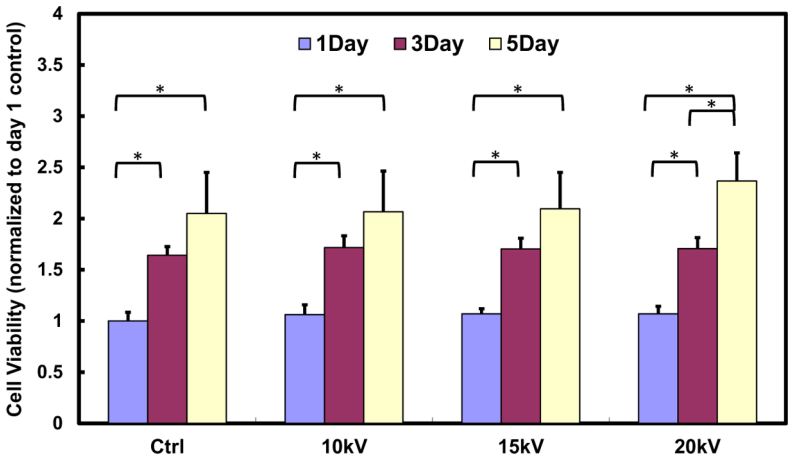

Fig. 1.
Viability of CDCs electrosprayed at different voltages (10, 15 and 20 kV).

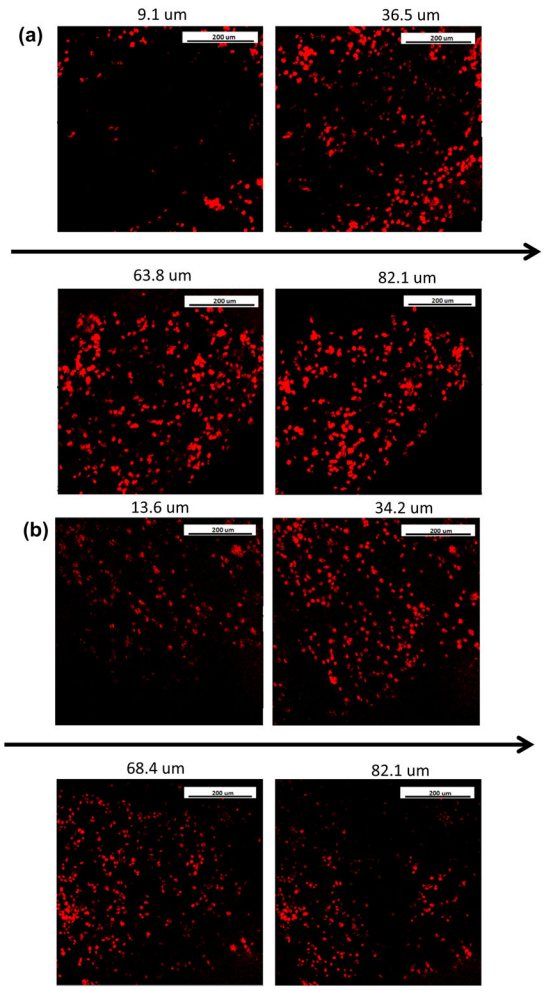

Fig. 2.
Distribution of cells of the tissue construct at different depths on day 1 (a) and day 7 (b).

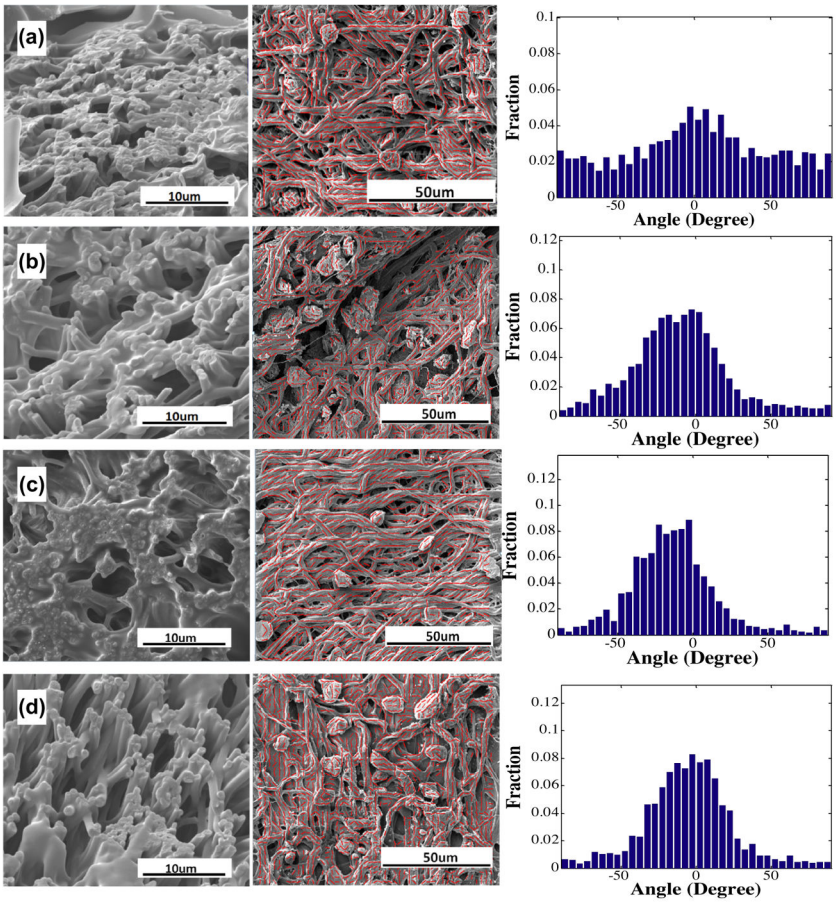

Fig. 3.

SEM images of tissue construct cross-sections, surfaces and fiber alignment/orientation distributions calculated based on the images. (a) HG9PU1/7.5; (b) HG9PU1/4.5; (c) HG7PU3/4.5; (d) HG5PU5/4.5.

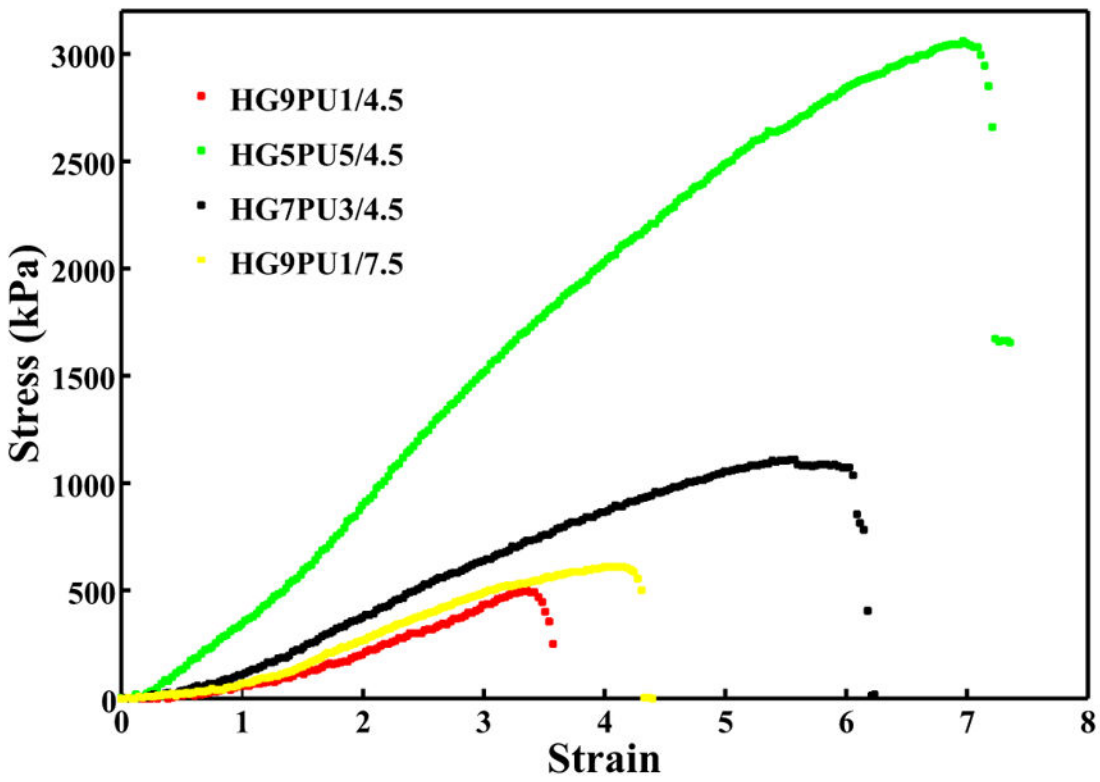

Fig. 4.

Representative stress–strain curves of the tissue constructs tested at 37 °C and in an aqueous condition.

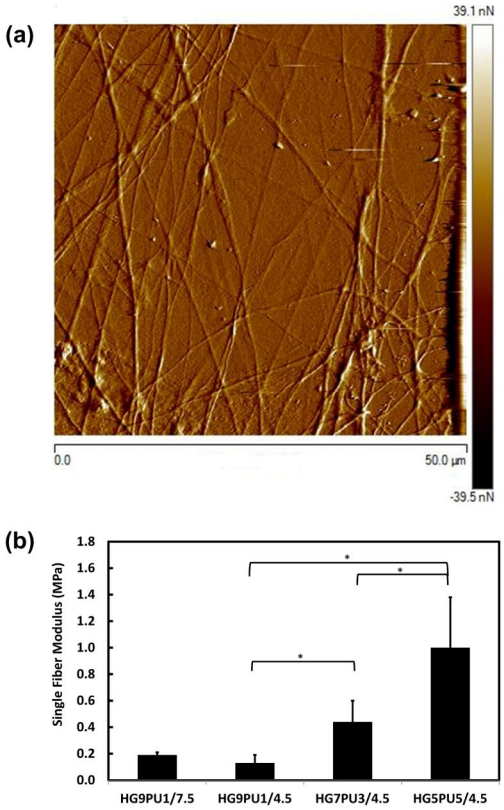

Fig. 5.
AFM characterization of scaffold morphology (a) and single-fiber modulus of scaffolds (b).

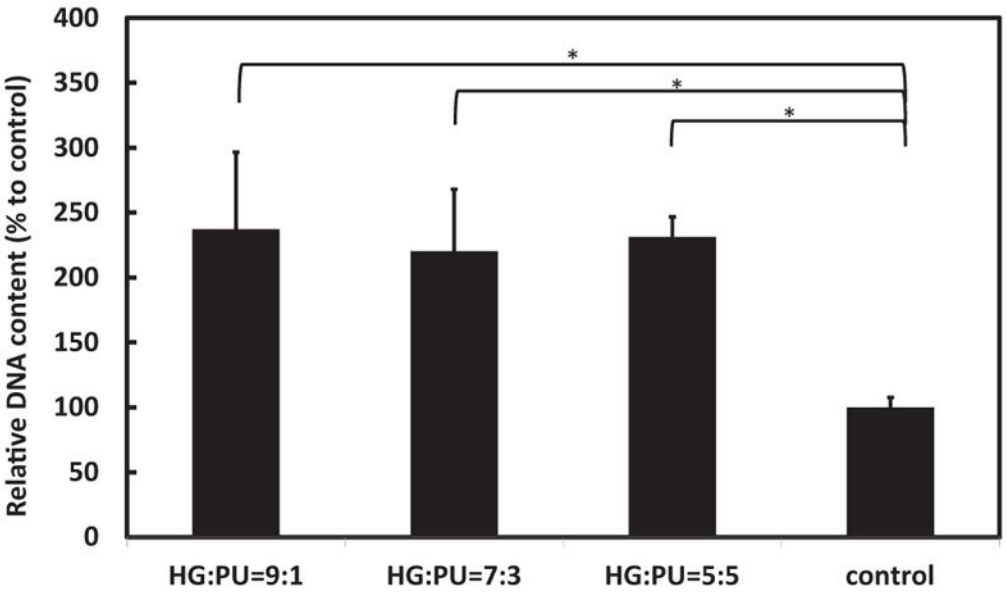

Figure 6.
CDC adhesion on 2-D films of hydrogel/polyurethane blends with different ratios.

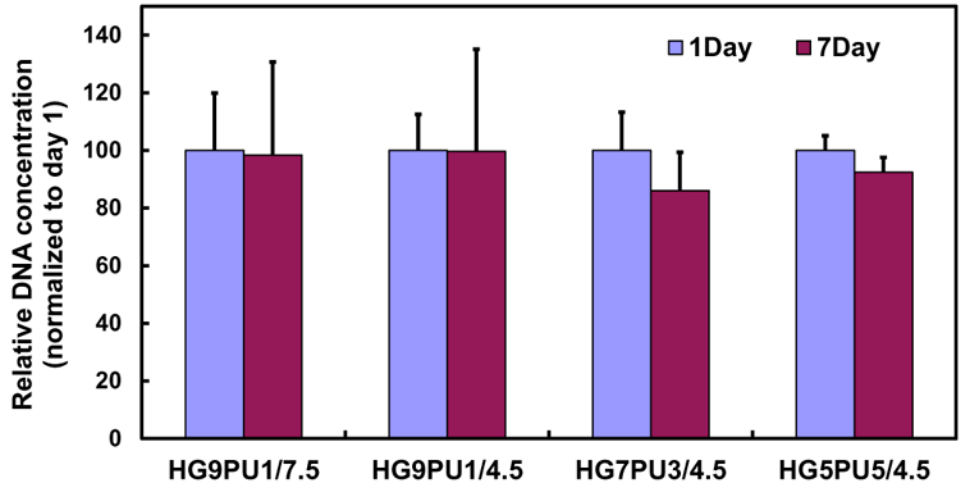

Fig. 7.
dsDNA content of tissue constructs after 1 and 7 days of culture in spinner flasks.

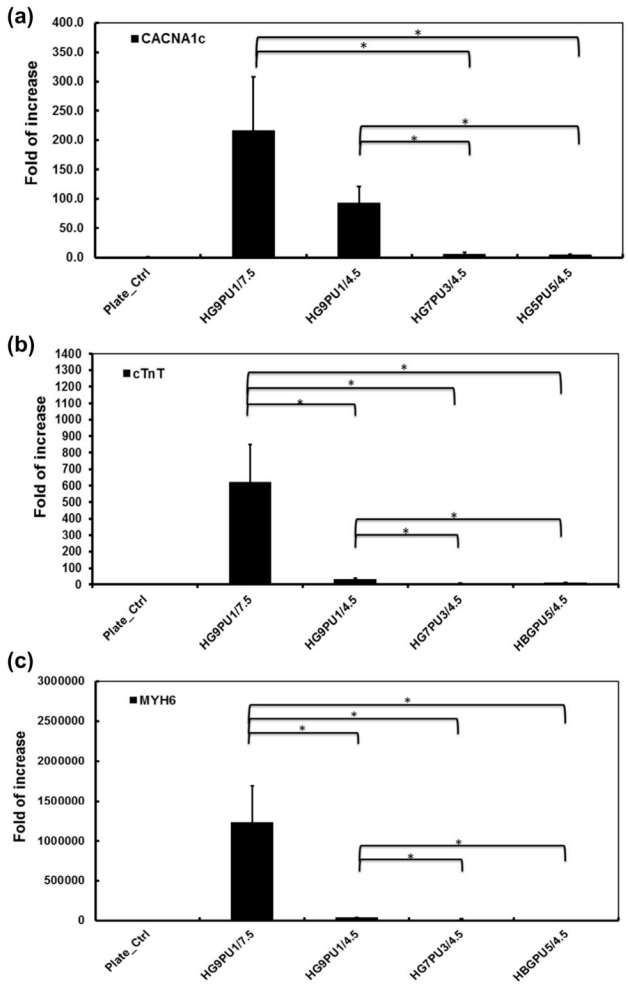

Fig. 8.

Gene expression of CDCs in tissue constructs after 7 days of culture in spinner flasks. (a) CACNA1c; (b) cTnT; (c) MYH6.

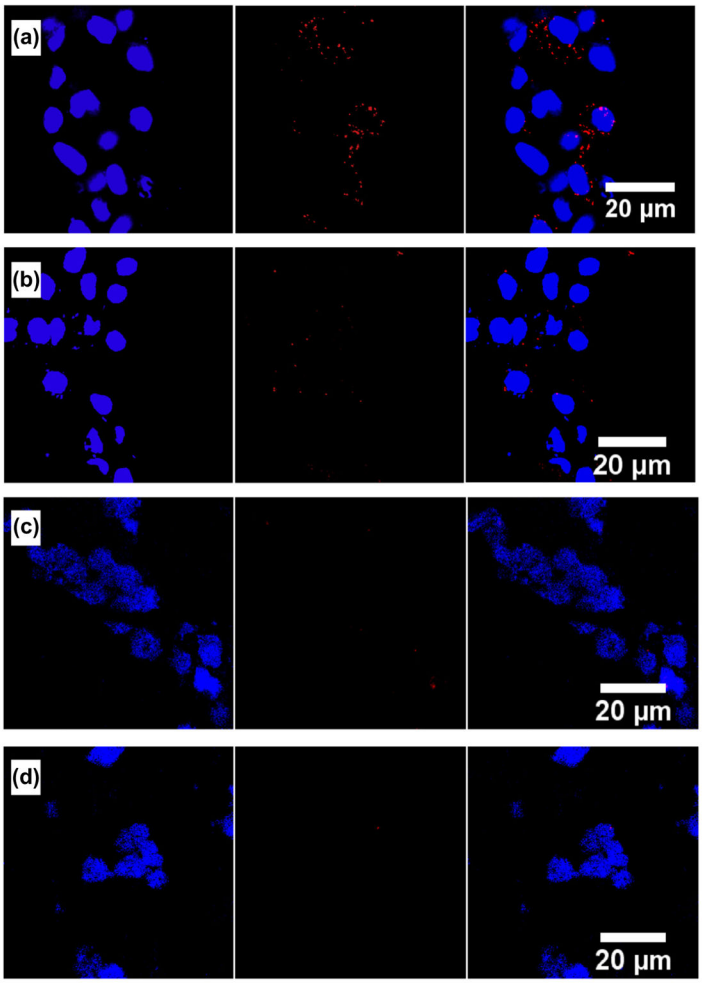

Fig. 9.

CX43 expression (red) of CDCs in tissue constructs after 7 days of culture in spinner flasks. Cell nuclei were stained by Hoechst (blue). (a) HG9PU1/7.5; (b) HG9PU1/4.5; (c) HG7PU3/4.5; (d) HG5PU5/4.5.

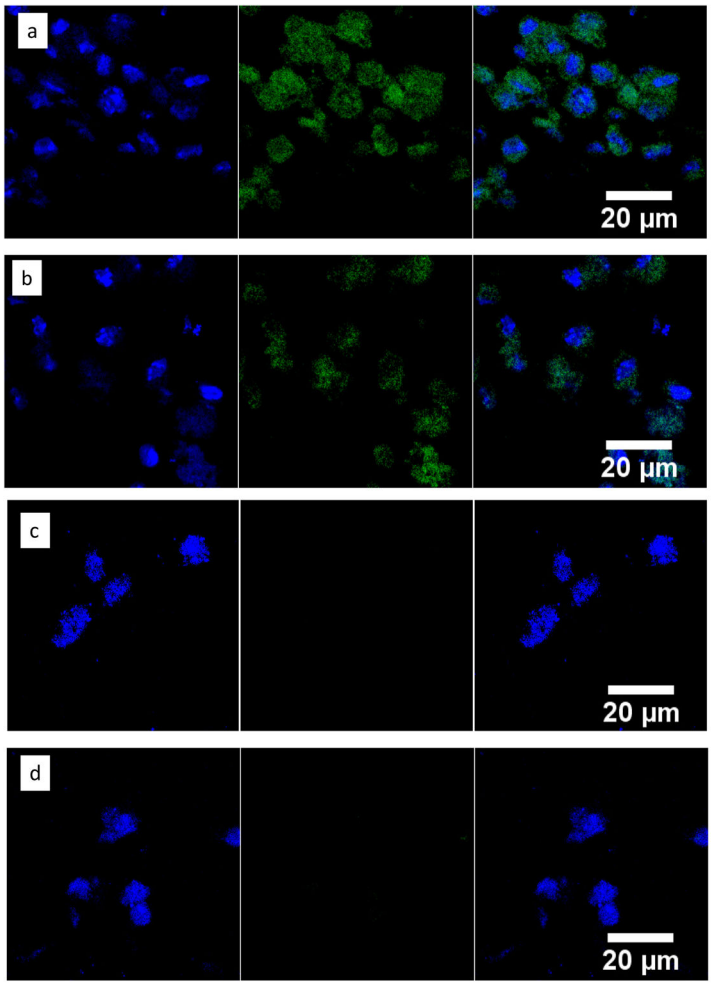

Fig. 10.

cTnI expression (green) of CDCs in tissue constructs after 7 days of culture in spinner flasks. Cell nuclei were stained by Hoechst (blue). (a) HG9PU1/7.5; (b) HG9PU1/4.5; (c) HG7PU3/4.5; (d) HG5PU5/4.5.

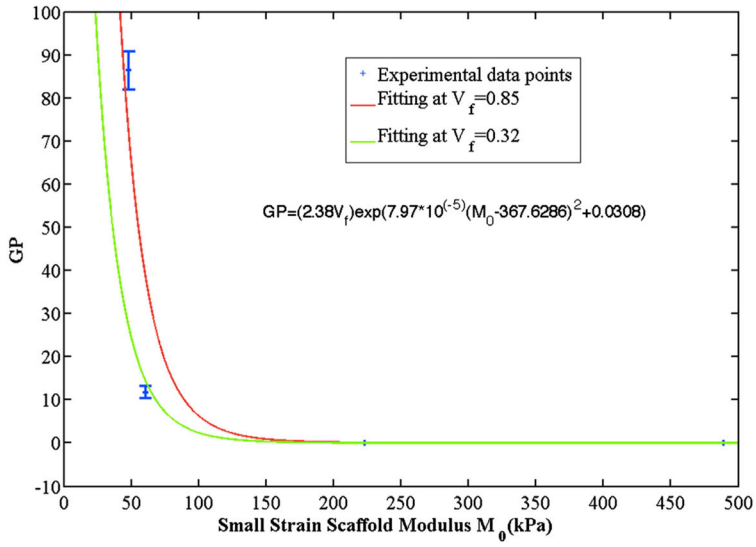

Fig. 11.

Simulated relationship of gene/protein expression (*GP*), fiber volume fraction (V_f), and small strain scaffold modulus (M_0).

Table 1

Fabrication parameters for tissue constructs.

Scaffold	Hydrogel content (%)	PU content (%)	Pumping speed (ml h^{-1})
(**A**) HG9PU1/7.5	90	10	7.5
(**B**) HG9PU1/4.5	90	10	4.5
(**C**) HG7PU3/4.5	70	30	4.5
(**D**) HG5PU5/4.5	50	50	4.5

Table 2

Primers used for real time RT-PCR.

Transcription	Prime sequences	T_m (°C)[a]
cTnT	Forward TACATCCAGAAGACAGAGCG	61.4
	Reverse CTCTCAGTTGGTCTTCATTCAG	60.7
MYH6	Forward GAGGAGATGCGAGATGAGAG	61.6
	Reverse CGGTTTGATCTTGAAGTAGAGC	61.3
CACNA1c	Forward CAGAAACTACAGGAGAAGAGG	59.5
	Reverse AAGAAGAGGATCAGGTTGGT	60.5
β-Actin	Forward AAGATCAAGATCATTGCTCCTC	61.2
	Reverse GGACTVATCGTACTCCTG	59.5

[a] T_ms were calculated by NIH PerlPrimer. cTnT, MYH6 and CACNA1c are cardiac specific markers cardiac troponin T, cardiac myosin heavy chain alpha, and calcium channel protein expressed in mature cardiomyocytes, respectively.

Table 3

Survival rate of CDCs after electrospraying.

Voltage (kV)	0	10	15	20
Survival rate (%)	97.2	97.7	97.6	98.9

Table 4

Fiber diameter, density, and alignment of different constructs.*

Scaffold	(A)	(B)	(C)	(D)
Diameter d (μm)	1.50 ± 0.12	1.28 ± 0.09	1.47 ± 0.22	1.37 ± 0.26
Density n (#/100 μm^2)	46.1 ± 2.0	25.5 ± 3.2	22.7 ± 2.8	22.2 ± 3.7
Alignment A_0	0.45 ± 0.06	0.61 ± 0.07	0.60 ± 0.02	0.59 ± 0.04

*Fiber diameter and density were detected by Image J based on the SEM images.

Table 5

Mechanical properties of different tissue constructs with cells on day 1.

Scaffold	(A)	(B)	(C)	(D)
Tensile modulus M_0 (kPa)	48.1 ± 10.9	60.4 ± 5.0	222.7 ± 32.5	463.1 ± 37.7
Tensile stress (kPa)	629.4 ± 97.5	440.8 ± 73.3	892.0 ± 67.3	2019.9 ± 283.9
Elongation	4.54 ± 0.87	3.62 ± 0.89	5.10 ± 0.69	7.17 ± 1.34

Table 6

Tensile moduli of different constructs without cells at days 1 and 7.

Scaffold	(A)	(B)	(C)	(D)
Tensile modulus at day 1 (kPa)	55.0 ± 1.4	60.4 ± 10.6	202.7 ± 17.9	421.8 ± 26.4
Tensile modulus at day 7 (kPa)	56.0 ± 2.1	57.4 ± 6.6	231.0 ± 31.9	425.8 ± 29.3

Table 7

A summary of process and response parameters of the tissue constructs.

Scaffold	Process parameters		Geometric and mechanical parameters					Functional response
	P[1]	H[2]	m_L[3]	A_0[4]	V_f[5]	M_0[6]	M_L[7]	GP[8]
(A)	7.5	90	2.0 ± 0.4	4.5 ± 0.5	8.5 ± 1.3	0.48 ± 0.11	1.7 ± 0.3	87 ± 4
(B)	4.5	90	3.5 ± 0.2	6.1 ± 0.7	3.2 ± 0.5	0.6 ± 0.05	1.2 ± 0.1	12 ± 1
(C)	4.5	70	9.0 ± 0.8	6.0 ± 0.2	4.2 ± 0.9	2.2 ± 0.3	3.9 ± 0.5	0.03 ± 0.00
(D)	4.5	50	26 ± 0.3	5.9 ± 0.4	3.1 ± 0.6	4.6 ± 0.4	8.1 ± 1.0	0.01 ± 0.00

[1] P: Polymer solution pumping speed (ml h^{-1});

[2] H: hydrogel content in fibers (wt.%);

[3] m_L: fiber modulus at large strain (Eq. (7)) (10^2 kPa);

[4] A_0: fiber alignment at small strain at v = 0.3 (Eq. (6)) (10^{-1});

[5] V_f: fiber volume fraction, $V_f = n \pi d^2/4$ (10^{-1};

[6] M_0: scaffold modulus at small strain (10^2 kPa);

[7] M_L: scaffold modulus at large strain (10^2 kPa);

[8] GP: gene and protein expression—gene and protein expressions were normalized first based on the results of real-time RT-PCR and immunohistology respectively, and then multiplied to give the GP value listed here.